Effect of cation rotation on charge dynamics in hybrid lead halide perovskites

Gélvez-Rueda, María C.; Cao, Duyen H.; Patwardhan, Sameer; Renaud, Nicolas; Stoumpos, Constantinos C.; Schatz, George C.; Hupp, Joseph T.; Farha, Omar K.; Savenije, Tom J.; Kanatzidis, Mercouri G.

DOI
10.1021/acs.jpcc.6b06722

Publication date
2016

Document Version
Accepted author manuscript

Published in
The Journal of Physical Chemistry C

Effect of Cation Rotation on Charge Dynamics in Hybrid Lead Halide Perovskites

Grozema, Ferdinand

Publication date
2016

Document Version
Peer reviewed version

Published in
The Journal of Physical Chemistry C

Citation (APA)
Grozema, F. (2016). Effect of Cation Rotation on Charge Dynamics in Hybrid Lead Halide Perovskites. The Journal of Physical Chemistry C, 120(30).

Effect of Cation Rotation on Charge Dynamics in Hybrid Lead Halide Perovskites

María C. Gélvez-Rueda[1], Duyen H. Cao[2], Sameer Patwardhan[2], Nicolas Renaud[1], Constantinos C. Stoumpos[2], George C. Schatz[2], Joseph T. Hupp[2,3], Omar K. Farha[2,4], Tom J. Savenije[1], Mercouri G. Kanatzidis[2,3], and Ferdinand C. Grozema[1]

[1] *Delft University of Technology, Delft, 2628BL, The Netherlands.*

[2] *Northwestern University, Evanston, IL 60208, United States.*

[3] *Materials Science Division, Argonne National Laboratory, Argonne, IL 60439, United States*

[4] *Department of Chemistry, Faculty of Science, King Abdulaziz University, Jeddah, Saudi Arabia*

Abstract

Organic-inorganic hybrid halide perovskites are a promising class of materials for photovoltaic application with reported power efficiencies over ~22%. However, not much is known about the influence of the organic dipole rotation and phase transitions on charge carrier dynamics. Here, we report substantial changes in mobility and lifetime of charge carriers in $CH_3NH_3PbI_3$ after the low temperature tetragonal (β) to orthorhombic (γ) phase transition. By using microwave conductivity measurements, we observed that the mobility and lifetime of ionized charge carriers increase as the temperature decreases and a sudden increment is seen after the β/γ phase transition. For $CH_3NH_3PbI_3$ the mobility and the half-lifetime increase by a factor of three to six compared with the values before the β/γ phase transition. We attribute the considerable change in the dynamics at low temperature to the decrease of the inherent dynamic disorder of the organic cation ($CH_3NH_3^+$) inside the perovskite crystal structure.

Introduction

Organic-inorganic halide perovskites have engendered a huge wave of effort in photovoltaic research community due to their ease of preparation methods and outstanding properties for a light absorbing material. The power conversion efficiency (PCE) of perovskite solar cells, $CH_3NH_3PbI_3$ in particular, has remarkably increased from 3.4% in 2009 to 22% in 2015.[1-6] This high efficiency is a result of outstanding semiconductor properties such as high absorption coefficient, high static dielectric constant, low effective mass of charge carriers, ambipolar charge-carrier mobilities and long carrier lifetime and diffusion length.[3] These properties have been mostly linked to the inorganic octahedral $(PbX_6)^{4-}$ sub-lattice as the organic cation does not have a direct influence on the construction of the valence and conduction bands.[7] Nevertheless, the optoelectronic properties and charge dynamics in perovskites can also be influenced by other mechanisms related to the size and the interaction of the organic cation with the crystal structure.[8 9-11]

The size of the organic cation has been shown to alter the optoelectronic properties, e.g. the bandgap, of AMX_3 halide perovskites due to the deformation caused to the perovskite crystal structure.[7,8,12] Moreover, the low symmetry and permanent dipole moment of the organic cation can result in a variety of orientations and rotational dynamics of this cation inside the PbX_6 octahedron. Measurements such as differential scanning calorimetry (DSC)[13,14], dielectric[15,16], infrared (IR) spectroscopy[13,14], nuclear magnetic resonance (NMR) spectroscopy[13], quasielectric[17] and high-resolution[18] neutron scattering, and 2D infrared vibrational spectroscopy[19] have confirmed the orientational disorder and rotation of the organic cation at room temperature. This rotational freedom is the most likely source of the high dielectric constant at low frequencies[16,20] in these materials. In addition, the inherent thermal (dynamic) disorder of the organic cation is intricately linked to the characteristic phase transitions that the AMX_3 perovskite class materials exhibit when the temperature is lowered. On cooling, the thermal motion decreases, leading to changes in the geometry of the unit cell and the formation of ordered domains.[13] These transitions have been observed by abrupt changes in calorimetry[13,14], dielectric measurements[15,16], IR[13,14] and NMR[13] spectroscopy measurements. The dynamics of the organic cations have been linked to the dielectric response[16], ferroelectric behavior[21,22], hysteresis in the I-V curves[23-25] and different electronic properties for polar or nonpolar isotropic configurations of the organic cations.[26]

Additionally, Monte Carlo simulations suggest the formation of ferroelectric domains below the β/γ phase transition temperature.[9,10,17] So far, the organic cation dynamics and characteristic phase transitions have not been correlated to fundamental semiconductor properties, such as mobility, lifetime, and recombination kinetics of charge carriers.

In this study, we report on the relationship between the organic cation dynamics, phase transitions and charge carrier properties in the bulk methylammonium (MA) lead halide perovskites, abbreviated as $MAPbX_3$ (X = I, Br). We use the unique pulse-radiolysis time-resolved microwave conductivity (PR-TRMC) technique to determine the mobility and lifetime of charge carriers at a variety of temperatures, covering the temperatures at which the perovskite phase transitions occur.[8,13] We observe abrupt changes in mobility and lifetime on going through the β/γ phase transition in contrast to a recent THz conductivity study.[27] These effects are attributed to changes in the dynamics of the organic cations. Reduction of the rotational motion of the organic cations in the orthorhombic (γ) low temperature phase creates a static energy landscape in which internal dissociation of charges reduces the extent of recombination, thereby increasing mobility and lifetime. Furthermore, we find that the bimolecular recombination rate decreases as the temperature decreases. This behavior is in contradiction with typical semiconductors behavior described by Langevin's theory.[28] We propose that different mechanisms, related to the dynamic disorder of the organic cations, influence the charge dynamics of hybrid halide perovskites.

Results and Discussion

PR-TRMC temperature dependent measurements

Pulse-Radiolysis Time-Resolved Microwave Conductivity (PR-TRMC) is a unique experimental technique that can be used on a wide variety of materials to determine the mobility and recombination kinetics of charge carriers. PR-TRMC measurements involve the generation of charge carriers through irradiation by a short pulse of high-energy electrons (3 MeV) and the monitoring of the changes in conductivity due to mobile charge carriers using high frequency microwaves (28-38 GHz).[29-31]

The high-energy electron pulse ionizes the material via ionization events that involve an average energy transfer of ~20ev. This results in the generation of a uniform concentration of charge carriers far away from each other. The thermal relaxations of the charges that are produced in this way occurs well within 100ps[32] and hence it does not influence recombination of the charges. Note that this is very different from laser photoconductivity measurements, such as TRMC and tera-Hertz spectroscopy, where charge carriers are generated very close to each other with a non-uniform concentration profile.[33] If the free charge carriers generated in this way are mobile, this results in a fractional absorption of microwave power reflected by the cell that is directly proportional to the change in conductivity of the material studied (Equation 1).[29-31]

$$\frac{\Delta P}{P} = A\Delta\sigma \quad (1)$$

The fractional change in the microwave power, $\Delta P/P$, and the sensitivity factor, *A*, are frequency dependent as the overlap of the electric field strength of the microwaves in the samples changes with frequency. In addition, interference effects of the incoming and reflected waves in the cell can also vary with frequency. The experimental frequency dependence of $\Delta P/P$ can be fitted with an analytical expression to determine the dielectric constant, ε, and change in conductivity, Δσ.[29-31] Information about trapping, recombination processes, and carrier lifetimes in the material can be determined from the temporal decay kinetics of the transients varying the initial concentration of charges in the material (by varying the length of the pulse).

Typical conductivity transients obtained by PR-TRMC measurements for polycrystalline bulk perovskites $MAPbX_3$ (X=I, Br) at different temperatures are shown in Figure **1**. The perovskite materials used in this study were prepared by reacting the MAX and PbX_2 salts via grinding and post-annealing as described in detail in the Supporting Information (SI). As can be seen in Figure 1, the change in the conductivity (Δσ) normalized by the irradiation dose is plotted as a function of time. The conductivity initially increases during the pulse as mobile charge carriers are generated and gradually decays after the pulse as the charges recombine or get trapped. The overall time response of the PR-TRMC set up is limited by the

rise time of the detector diode and the length of the excitation pulse but is less than 1 ns; i.e. much shorter than the lifetime of the conductivity signals. The mobility of the charges can be determined from the change in the conductivity (Δσ) if the charge carrier concentration at the end of the electron pulse (N_p) is known (Equation 2).[29-31] Since it is not possible to selectively generate positive or negative charges, the mobility determined by PR-TRMC technique is the sum of the electron and hole mobilities.

$$\Delta\sigma = e \sum N_p(0)\, \mu = e\,(n_n\mu_n + n_p\mu_p) \qquad (2)$$

Overall, the conductivity (mobility) and lifetime increase when the temperature decreases as can be seen in Figure 1. Noticeably, when the $MAPbI_3$ compound goes through the phase transition from tetragonal (β) to orthorhombic (γ) at around -115°C, not only does the conductivity increase but also the carrier lifetime becomes much longer. The change in lifetime for $MAPbBr_3$ is much smaller. The conductivity is very similar for both $MAPbI_3$ and $MAPbBr_3$.

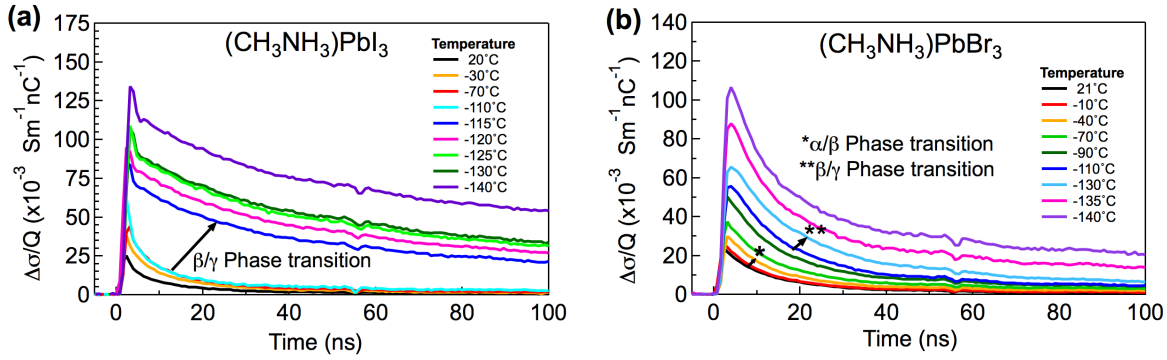

Figure 1. Conductivity transients of $CH_3NH_3PbI_3$ (a) and $CH_3NH_3PbBr_3$ (b) at different temperatures.

To further illustrate the carrier dynamics, we plot the mobility and conductivity half-lifetime as a function of temperature in Figure 2 for both $MAPbX_3$ (X = I, Br) compounds. At room temperature, the charge carrier mobilities are ~1-2 $cm^2V^{-1}s^{-1}$ for $MAPbI_3$ and $MAPbBr_3$, respectively. In the case of $MAPbCl_3$, the mobility is one order of magnitude lower. We speculate that this lower mobility is caused by a higher concentration of intrinsic defects (see SI for further discussion). [34,35] The mobility values for the mixed halides ($MAPbI_2Br$ and $MAPbIBr_2$) are very similar and can be found in the SI. Although going from $MAPbI_3$ to

$MAPbBr_3$ reduces the size of the perovskite unit cell and increases the optical band gap (see SI for the XRD and absorbance spectra), the effect on the mobility of charges in the material is not significant.

Charge carrier mobility of spin coated $MAPbI_3$ thin films determined by transient tera-Hertz spectroscopy and microwave photoconductivity has been shown to be ~6-35 $cm^2V^{-1}s^{-1}$. [27,36-39] Note that the charge carrier mobilities reported here are lower than the previously reported values.[27,36-39] Our relatively lower mobility could stem from an overestimation of the number of charge carriers produced in the current experiment. We speculate that the radiation-ionization energy required for the generation of an electron-hole pair (E_p) in hybrid perovskites may be higher than that in typical semiconductor materials.[40,41] Moreover, different perovskite bulk sample morphologies could also lead to different mobility results. For instance, the bulk polycrystalline materials (see Figure S3 in SI) that we used in this study exhibit small domain sizes (nm to μm scale), which increases the probability of recombination of the charge carriers and decreases their mobility.

In Figure 2 it is clear that the mobility increases at lower temperatures for both $MAPbI_3$ (Figure 2a) and $MAPbBr_3$ (Figure 2b). In contrast to a previous study[27], an abrupt change is observed in the mobility trend upon going through the tetragonal to orthorhombic (β/γ) phase transition. As a consequence, down at -130°C the mobility reaches values of ~6 $cm^2V^{-1}s^{-1}$ for $MAPbI_3$ and $MAPbBr_3$.

For $MAPbI_3$ (Figure 2a) the mobility and lifetime do not exhibit abrupt changes around the cubic to tetragonal (α/β) phase transition at 57°C. In the temperature range between 90°C down to -110°C, the temperature dependence of the mobility follows band–like transport behavior characteristic of classic semiconductors such as silicon ($\mu=T^{-1.5}$).[42] In addition, the half-lifetime slightly decreases. Both trends are consistent with reduction of phonon scattering or lattice vibrations of the inorganic $(PbX_6)^{4-}$ framework at lower temperatures. Acoustic phonon-electron scattering behavior in $MAPbI_3$ has also been recently reported.[27,43] Interestingly, at temperatures below -110°C sudden changes in mobility and lifetime are observed. This sudden change coincides with the transition from the tetragonal

to orthorhombic phase (β/γ) in $MAPbI_3$ and is therefore intricately linked to the structural changes. We observed the effect of this transition as the mobility increases following a strong deviation from the acoustic phonon scattering behavior ($\mu = T^{-1.5}$); and the half-lifetime shows a sudden rise that continues increasing as the temperature decreases further.

The behavior of $MAPbBr_3$ is similar to $MAPbI_3$. Significant changes in mobility and lifetime are not observed when the temperature is around the α/β phase transition (-36°C). Around these phases, the mobility gradually increases following band–like transport behavior. After the β/γ phase transition (-124°C) the mobility suddenly rises and the half-lifetime slightly increases. The half-lifetime increment is obscured at low temperature due to fast trapping of charges during the first 10 ns. This behavior will be further discussed below where the recombination and trapping dynamics of the charges are analyzed.

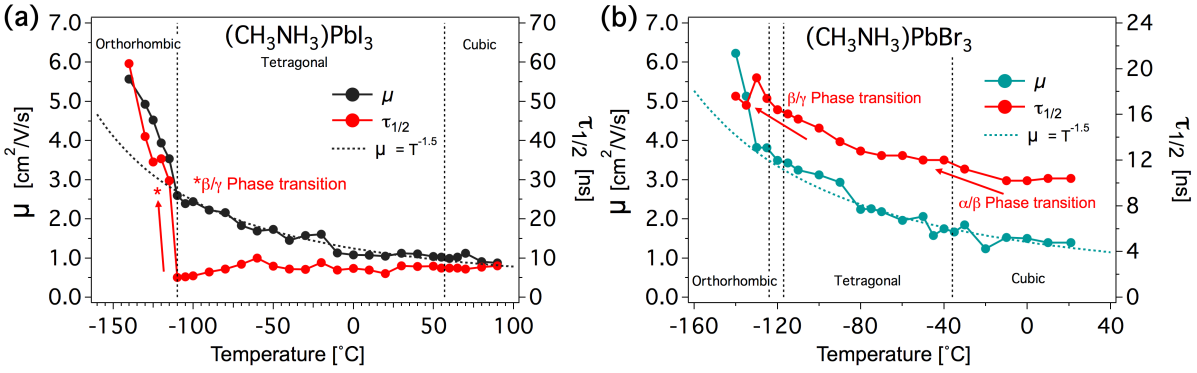

Figure 2. Mobility and half-life time for $CH_3NH_3PbI_3$ (a) and $CH_3NH_3PbBr_3$ (b) at different temperatures.

From our results it is clear that below the tetragonal to orthorhombic (β/γ) phase transition temperature in $MAPbI_3$ and $MAPbBr_3$ the charge carrier dynamics change abruptly. This sudden variation cannot be attributed entirely to the reduction of the phonon scattering, but other dynamics inside the crystal structure should also be taken into account. We argue that these different dynamics are related to the dynamic disorder of the organic cation.

The rotational freedom of the MA^+ cation in the perovskite crystal lattice has been confirmed by several techniques.[13-15,17-19] More recently, the real-time motion was

measured at room temperature by 2D-IR vibrational anisotropy spectroscopy[19] and at room and lower temperatures by high-resolution neutron scattering.[18] Overall, these studies conclude that at room temperature and above there is substantial rotational freedom and the organic cation constantly reorients. Lowering the temperature reduces the motion of the organic cation, leading to phase transitions in the crystal structure.[13-15] Transitioning from the cubic to tetragonal (α/β) phase, the organic cation preserves its dynamic disorder. But below the tetragonal to orthorhombic (β/γ) phase transition temperature its orientation becomes fixed. This restriction has been observed by dielectric spectroscopy[15,16], NMR measurements[13], high-resolution neutron scattering[18] and a variety of computational studies.[9,10,17,19] The rotational motion of the organic cation influences the dielectric constant and internal electric field of the material.[16] As a consequence, it can directly influence the charge carrier dynamics.[19,44] This influence is observed in our temperature dependent PR-TRMC measurements.

When the perovskite lattice is in cubic phase (room to higher temperatures), the time for the rotation of the organic cation is of the order of ~0.3 ps for a wobbling-in-a-cone motion and ~3 ps for 90° jumps.[19] Such fast rotation creates a relatively homogeneous disordered (non-ferroelectric) energy landscape where electrons and holes easily recombine, decreasing the lifetime of charge carriers. As the temperature decreases, the movement of the organic cation reduces, inducing the transition to the tetragonal (β) phase. However, in the β phase the organic cation preserves its rotational freedom. This is observed by high-resolution neutron scattering measurements[18] in which the average mean-squared displacement of the hydrogen atom of the organic cation ($\langle u^2 \rangle$) remains at the same order of magnitude on going through the α/β phase transition, but abruptly decreases below the β/γ phase transition temperature. This explains why in our PR-TRMC measurements the mobility does not exhibit a sudden change on going through the α/β phase transition, but continues to follow a band-like behavior.

Below the β/γ phase transition temperature in $MAPbI_3$ and $MAPbBr_3$ the mobility and lifetime abruptly increase. We attribute this sudden change to the restriction in the movement of the organic cations. Due to the reduced rotational motion, the dynamically

disordered energy landscape at room temperature is replaced by a static one. At room temperature the 3ps 90° jumps[19] occur in the same time order of the charge transport, affecting the recombination and decreasing the mobility and lifetime. At low temperature, this jump rotation becomes completely static, resulting in a higher mobility and a very long lifetime of the charges. This is a consequence of the high dipole moment of MA^+, leading to separate areas in the material that are favorable for either the electrons or the holes. This transport mechanism has been theoretically proposed in hybrid halide perovskites[9], suggesting that in a material with multi-domain regions, the charges diffuse to domain boundaries and through the potential generated by the local dipole (minima for the electrons, maxima for the holes). This internal dissociation of charges reduces recombination, increasing mobility and lifetime. Other calculations with specific dipole orientation show that these charge domain walls can occur and may lead to reduced recombination rate.[45,46] Additionally, in device modeling studies it has been shown that dipole alignment can result in separate channels for transport of electrons and holes with reduced recombination.[11] The proposed effects described here are consistent with the sudden rise in mobility and lifetime exhibited in our measurements by $MAPbI_3$ and $MAPbBr_3$ below the β/γ transition temperature.

In order to further test the influence of the organic cation on the charge dynamics, we performed similar PR-TRMC measurements on an inorganic based perovskite: $CsPbBr_3$. $CsPbI_3$ was not tested as the temperatures at which its black cubic perovskite phase is stable (T>310°C)[8,47] are out of our experimental possibilities. The absence of a dipole moment in the inorganic cation, Cesium (Cs), allows us to assess the effect of the phase transitions and the freezing of the organic cation on the $MAPbBr_3$ charge carrier dynamics. We determined the mobility and half-lifetime of $CsPbBr_3$ in a temperature range between -140°C and 180°C. $CsPbBr_3$ phase transitions occur at 130°C, cubic to tetragonal (α/β), and at 88°C, tetragonal to orthorhombic (β/γ).[48] As a consequence, $CsPbBr_3$ is in the orthorhombic phase at room temperature and remains in this phase at temperatures down to -260°C.[48] The mobility and half-lifetime of $CsPbBr_3$ against temperature are shown in **Error! Reference source not found.** in SI. In this figure it can be seen that the charge carrier mobility does not exhibit abrupt changes on going through the α/β and β/γ phase transitions. In fact, the mobility

behavior with temperature for $CsPbBr_3$ does not exhibit strong deviations from the acoustic phonon-electron scattering behavior of normal semiconductors ($\mu=T^{-1.5}$) in the temperature range tested. In the case of the half-lifetime, it does not exhibit abrupt changes on going through the phase transitions. Nevertheless, it varies along the temperature range, especially around room temperature. These results seem to indicate that the dynamics in $CsPbBr_3$ are only influenced by the vibrations of the lattice, local inorganic $(PbX_6)^{4-}$ framework and extended $[PbX_3]^{1-}$ framework, as the temperature is varied. This is in agreement with our proposal that the rotation and subsequent freezing of the organic cation influence the charge dynamics in $MAPbBr_3$ causing abrupt changes in the mobility.

Charge recombination and trapping

In Figure 3 and Figure 4 the experimental (a,b) and fitted (c,d) radiation induced conductivity of $MAPbI_3$ and $MAPbBr_3$ at room and low temperature are plotted against time for different initial concentration of charges (directly proportional to the length of the pulse). An offset of the x-axis is included in Figure 3 and Figure 4 in order to clearly show the differences in the end-of-pulse conductivity for the different pulse lengths. The pulse length was varied from 0.2 ns to 1 ns, resulting in an initial concentration of carriers from ~$4x10^{14}$ cm^{-3} to ~$4x10^{15}$ cm^{-3}. These pulse induced charge carrier concentrations are much lower than those generated under a standard solar simulator with 1.5 AM illumination conditions (10^{16}-10^{17} cm^{-3}).[49,50] Nevertheless, the low intensities available in our experiment allow us to observe the charge dynamics of hybrid perovskites at different conditions which are not feasible in transient tera-Hertz spectroscopy and microwave photoconductivity experiments,[27,37-39] where the high intensities of laser generate higher initial concentrations of charge carriers up to ~10^{18} cm^{-3}.[27]

The experimental transient data (Figure 3a and 4a) show that the conductivity decays faster for higher initial concentration of charges, which is consistent with the second-order charge recombination behavior. Nevertheless, the end-of-pulse conductivity also increases for longer pulses. This is not expected for pure second-order kinetics where the recombination of charge carriers during the pulse should be faster for higher concentrations, leading to the same or a lower end-of-pulse conductivity. This behavior points to the presence of a limited concentration of trap states in the material for either the electron or the hole. When low

concentrations of charges are created, all traps are rapidly filled. This is observed, especially in the 0.2 ns pulse, in the lower end-of pulse conductivity and the fast initial decay (t < 10ns), followed by a slower decay that is attributed to the opposite charge. When more charges are generated, all the traps become occupied and the remaining charges are free to move after the pulse (resulting in higher end-of-pulse conductivity), but recombine faster with the opposite charge.

In addition, the pulse lengths chosen during our experiments allow us to observe the saturation of the trap states in the material as the initial concentration of charge carriers is varied below and above the trapping density. The saturation, or complete filling, of the trap states is observed at the highest concentration of charges generated with a pulse length of 1 ns. This behavior is clear for $MAPbBr_3$ in Figure 4a and 4b where a lower conductivity with the 1 ns pulse is observed at both room temperature and -130°C. The second-order recombination and decay are faster as more charges are in the bulk after the traps have been filled. For $MAPbI_3$, complete trap filling is observed for the 1 ns pulse at low temperature. In this material, the presence of trap states is well illustrated in the extremely rapid initial decay of the 0.2 ns pulse. After 10 ns, the decay is much slower (almost horizontal) than that for longer pulses.

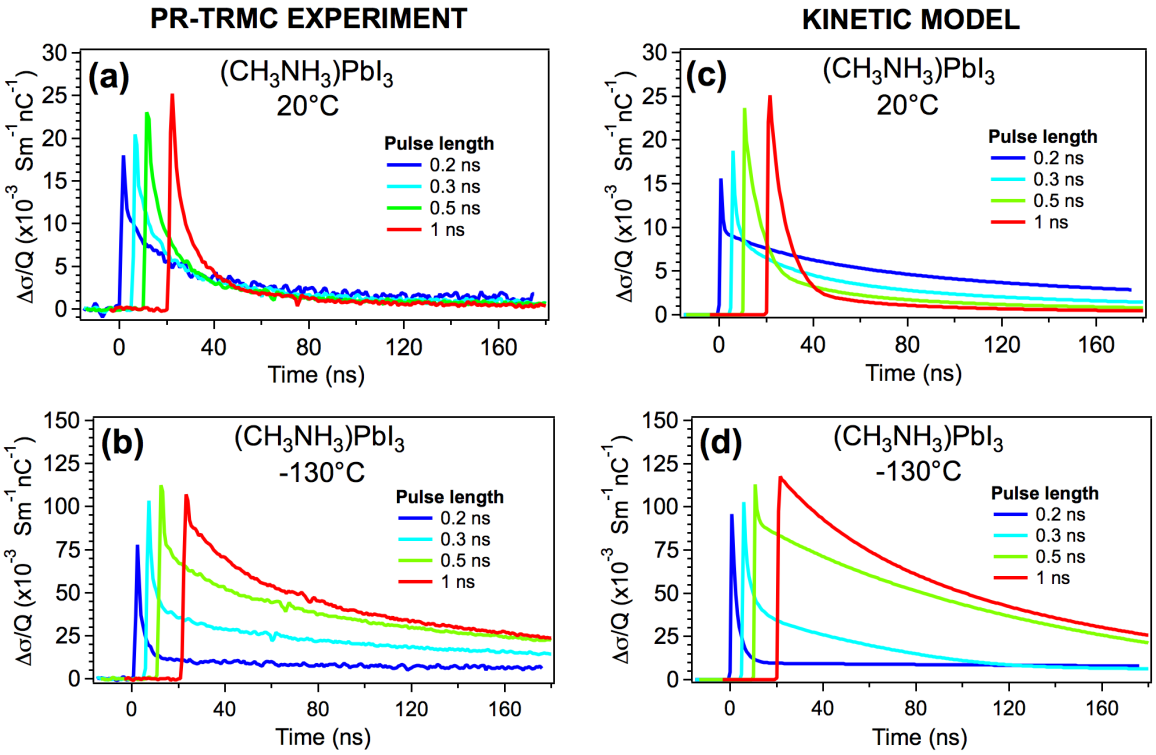

Figure 3. Experimental (a,b) and kinetic model fit (c,d) Pulse length dependence of $CH_3NH_3PbI_3$ at room (top) and lower (bottom) temperatures

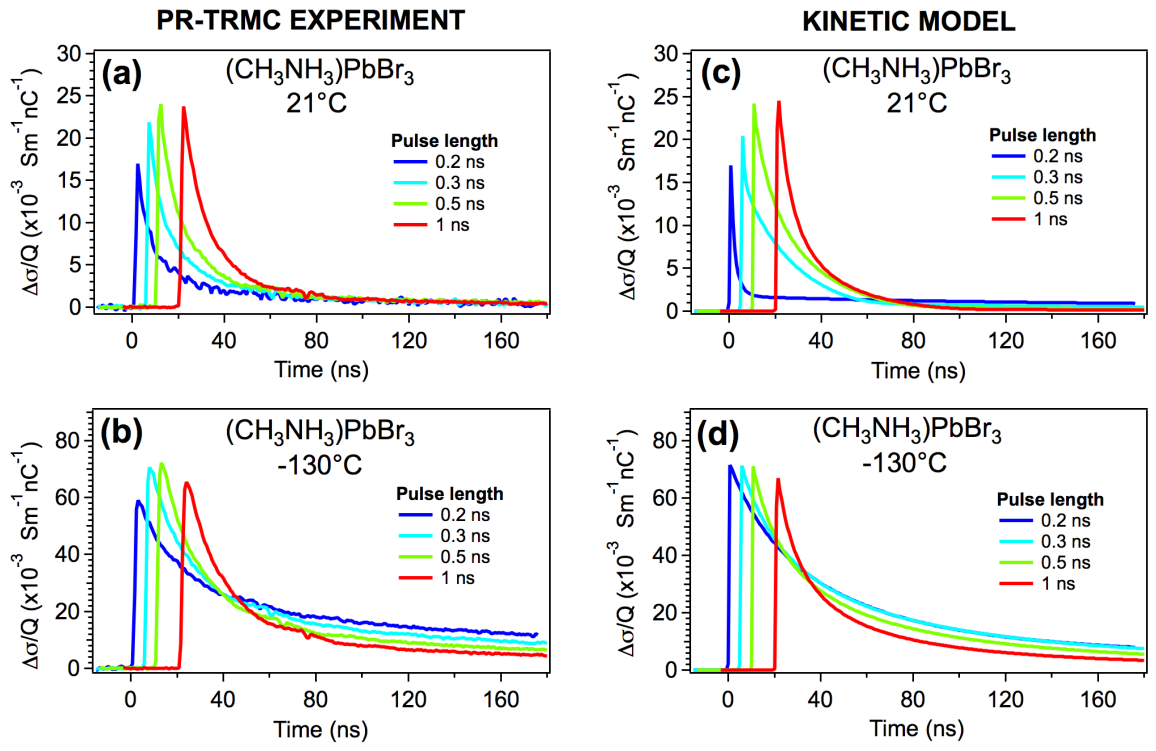

Figure 4. Experimental (a,b) and kinetic model fit (c,d) pulse length dependence of $CH_3NH_3PbBr_3$ at room (top) and lower (bottom) temperatures

In order to confirm our hypothesis and derive information on the trap concentrations, we have fitted the experimental pulse length dependence of $MAPbI_3$ and $MAPbBr_3$ to a charge carrier kinetics model that is analogous to previously reported models.[39,51] Based on the experimental data, the model we used includes the following processes:

- Generation of charge carriers **(1)**,
- Second-order bimolecular recombination (radiative recombination function of the amount of charges created) **(2)**,
- Second-order charge trapping with a limited concentration of traps (trap filling is a function of the trap concentration) **(3),** and
- Second-order recombination with trapped charges **(4)**.

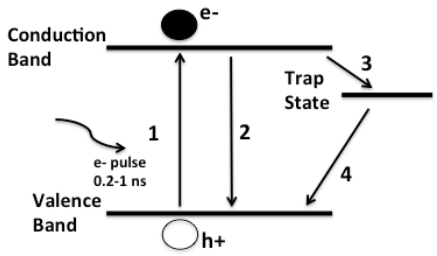

Figure 5. Schematic charge carriers' dynamics model

A schematic representation of this kinetic model is shown in Figure 5. We propose an approximated two-level model due to low occurrence of Auger processes and the very fast time scale at which thermal relaxation of the charges to the band edges occurs (100ps[32]). We have discarded the possibility of Auger recombination in the model due to the low concentration of charges created (10^{14} - 10^{15} cm^{-3}) in our experiment, since Auger processes are significant only at high charge carrier concentrations (10^{18} cm^{-3}).[27] A more detailed description of the kinetic model, the resulting differential equations and the determination of the change in conductivity with time are given in the SI. The results of this analysis for the pulse length dependent measurements for $MAPbI_3$ and $MAPbBr_3$ are shown in Figure 3 (c,d) and Figure 4 (c,d), respectively. The kinetic parameters, rate constants and mobility, used to solve the model for both samples are listed in Table 1.

Table 1. Kinetic fitting parameters for $CH_3NH_3PbI_3$ and $CH_3NH_3PbBr_3$ at 20°C and -130°C

Perovskite	$CH_3NH_3PbI_3$		$CH_3NH_3PbBr_3$	
Description/Temperature	20°C	-130°C	20°C	-130°C
Mobility: e- / h+ [cm^2/V/s]	1.12 / 0.4	5.5 / 0.4	1.7 / 0.1	3.7 / 0.4
Generation yield (k_1) [1/cm^3/nC]	1.51E+15	1.51E+15	1.12E+15	1.12E+15
Second order recombination rate (k_2) [cm^3/s]	3.00E-08	2.00E-09	4.00E-08	1.90E-08
Second order trap filling rate (k_3) [cm^3/s]	1.90E-06	7.00E-07	2.50E-06	6.40E-08
Second order trap emptying rate (k_4)	2.50E-08	2.50E-09	1.50E-08	2.00E-10
Trap state concentration N_t [1/cm^3]	1.40E+15	9.80E+14	5.00E+14	4.00E+14

As seen in Figure 3(c,d) and Figure 4(c,d), the kinetic model we propose accurately describes the main features of the conductivity decays. This demonstrates that the effects seen in our experimental transients are consistent with the presence of a limited concentration of trap states in the material. Additional processes such as photodoping of charge carriers into subgap states[51] or the presence of background charges[39] are likely to occur and may improve the accuracy of the fits. However, we chose to use the simplest model that describes the main features observed. The total mobilities used for the fits (Table 1) are in good agreement with the values displayed in Figure 2. Somewhat higher mobility values can be expected from the model as the experimental signals are limited by recombination during the pulse. The features in the experimental conductivity decay in Figure 3(a,b) and Figure 4(a,b), suggest that the mobility of the individual charges (electrons/holes) is considerably different. This is observed, especially at low temperature for $MAPbI_3$, in the fast initial trapping of one of the charges and subsequent slow decay of the other.

Our DFT band structure calculations predict that the mobility of the holes was slightly (~1.3-2 times) higher than the mobility of the electrons. However, we defined in our kinetic model that the trap states have an electronic nature.[39,51,52] As the most mobile charge gets trapped first, the mobility of the electrons is higher than for the holes. It should be noted that the nature of the trap states (either electrons or holes) is not known. In our experiment we cannot discriminate between the positive and negative charges and the reverse situation is also mathematically valid. Although the nature of the traps is not known, we deducted that

the concentration of trap states (N_t) is ~1x10^{15} cm^{-3} for $MAPbI_3$ and ~5x10^{14} for $MAPbBr_3$. These trap concentrations are high considering that the concentrations of charges generated by our experiments are of the same order of magnitude. This landscape makes the second order trap-filling rate (k_3) dominant over the recombination (k_2) and trap emptying (k_4) rates.

In order to compare our results to previously reported monomolecular recombination rates determined by PL decay measurements in thin films[27] we multiplied the second-order trap-filling rate (k_3) with the concentration of trap states (N_t) determined by our model. For $MAPbI_3$, our calculated monomolecular recombination rate is 2.66 x 10^9 s^{-1} at 20°C and 6.86 x 10^8 s^{-1} at -130°C. These values are two orders of magnitude faster than the previously reported ones.[27] The difference is presumably related to the morphology of the samples as the concentration of trap states is higher in polycrystalline bulk samples (grain size ~nm to µm scale, see SEM image in the SI) than in thin films. Still, the temperature trend is the same. As the temperature increases the monomolecular recombination rate increases. This behavior may be related to charge recombination with ionized impurities (originated from vacancies, substitutions or interstitials).[27] The second-order recombination rate (k_2) decreases as the temperature decreases from 3 x 10^{-8} cm^3 s^{-1} at 20°C to 2 x 10^{-9} cm^3 s^{-1} at -130°C. This trend is in agreement to microwave photoconductivity measurements[37], but in contradiction to the Langevin's trend of bimolecular recombination rate determined using optical-pump-THz probe spectroscopy.[27]

Direct comparison between PR-TRMC and tera-Hertz spectroscopy, however, is hampered by differences in the time scale of the analysis (1.5 ns in THz spectroscopy to 200 ns in PR-TRMC) and the electric field strength (~150 kV/cm[53] in THz spectroscopy to <100 V/cm[30] in PR-TRMC). Processes that occur on a sub-nanosecond timescale are not explicitly observed in the PR-TRMC experiments. The much higher electric fields can also have an influence in the mobility of the charges.

The observed deviation from the theory of Langevin can be explained by the effect of the disorder introduced by the dynamic rotational disorder of the organic cations. Langevin's theory states that the probability of electron-hole recombination should increase at low

temperature, as the velocity (mobility) at which an electron approaches to the Coulombic capture radius of the hole is higher and the thermal energy available to escape is lower.[28] We propose that the charge carrier dynamics in these hybrid halide perovskites are influenced by different mechanisms that are not considered in Langevin's theory. As discussed above, the freezing of the organic cation after the β/γ transition at low temperature creates local polarized domains for example. These domains lead to efficient dissociation of opposite carriers, allowing the charges to move away from the Coulombic capture radius. This process increases the lifetime of charge carriers and reduces the second order recombination.

In the case of $MAPbBr_3$ similar trends are observed. The monomolecular recombination decreases with temperature from 1.25 x 10^9 s^{-1} at 20°C to 2.56 x 10^7 s^{-1} at -130°C. For this compound the trapping rate is slower and the number of traps lower compared to $MAPbI_3$. The second-order recombination rate also decreases with temperature from 4 x 10^{-8} cm^3 s^{-1} at 20°C to 1.9 x 10^{-8} cm^3 s^{-1} at -130°C. This is consistent with the influence of the freezing of the organic cation on the charge carrier dynamics. The rate for second order recombination in $MAPbBr_3$ is higher than for $MAPbI_3$. This is a consequence of the lower concentration of trap states in $MAPbBr_3$, which diminishes the trapping effects.

Concluding remarks

To conclude, PR-TRMC measurements were used to determine the charge carrier dynamics in bulk $CH_3NH_3PbX_3$ (X= I, Br) perovskites at different temperatures. We observed that the charge carrier dynamics in hybrid perovskites are influenced by different mechanisms than the phonon-electron scattering or reduction of lattice vibrations commonly present in semiconductors. We propose that these different processes are related to the rotational freedom of the organic cation at high temperature and subsequent freezing below the tetragonal (β) to orthorhombic (γ) phase transition temperature.

At temperatures above the β/γ phase transition, the charge dynamics are dominated by the vibrations of the lattice, local inorganic $(PbX_6)^{4-}$ framework and extended $[PbX_3]^{1-}$ framework, following band-like transport behavior. The organic cations do not have much influence on the dynamics, as at these temperatures their reorientation is very fast; creating

a homogeneous energy landscape in the material. Upon going through the β/γ phase transition, the charge carrier dynamics abruptly change, deviating from band-like transport behavior characteristic of common semiconductors. The abrupt increase in mobility and lifetime observed is consistent with the freezing of the organic counter-ions in the structure; such fixed cation position creates a static energy landscape in which local polarized domains enhance charge separation, thus reducing recombination and increasing the mobility and lifetime of the charges in the materials. In addition, the influence of the organic cation dynamic disorder is also seen in the decay kinetics. The decrease of the bimolecular recombination at low temperature, in contradiction to Langevin's theory, is associated with the fixed position of the organic cation in the orthorhombic phase.

The absence of abrupt changes on going through its phase transitions and band-like transport behavior of the charge dynamics in the all-inorganic based $CsPbBr_3$, supports the conclusion that the abrupt change in mobility observed in $MAPbBr_3$ is related to the rotation and subsequent freezing of the organic cation in the orthorhombic phase.

Furthermore, the decay of conductivity with time of $CH_3NH_3PbX_3$ (X= I, Br) can be well described by our charge carrier kinetics model and indicates that the charge dynamics follow a second order recombination of charge carriers in the presence of a limited concentration of trap states. The nature of the trap states in the material is still not known but we estimate their concentration to be ~$1x10^{15}$ for $CH_3NH_3PbI_3$ and $5x10^{15}$ cm^{-3} for $CH_3NH_3PbBr_3$.

Finally, the technique used in this work gives a powerful insight into the charge dynamics of materials. Using PR-TRMC we can excite charge carriers far away from each other and determine their mobility and its trend with temperature independent of the wavelength energy. In our opinion, determine the mobility based in only the analysis of photoconductivity measurements is not sufficient. Particularly in temperature dependent measurements. At very low temperature the thermal energy available decreases and can not be sufficient for the charges generated by laser excitation to dissociate. This is a consequence of how close together the charges are generated in this type of measurements.

Acknowledgments

The research leading to these results has received funding from the European Research Council Horizon 2020 ERC Grant Agreement no. 648433. The work at Northwestern University was supported as part of the Argonne-Northwestern Solar Energy Research (ANSER) Center, an Energy Frontier Research Center funded by the U.S. Department of Energy, Office of Science, Office of Basic Energy Sciences, under Award Number DE-SC0001059. D.H.C. acknowledges support from the Link Foundation through the Link Foundation Energy Fellowship Program.

References

(1) Kojima, A.; Teshima, K.; Shirai, Y.; Miyasaka, T. *Journal of the American Chemical Society* **2009**, *131*, 6050.

(2) (NREL), N. R. E. L. **2016**.

(3) Gao, P.; Gratzel, M.; Nazeeruddin, M. K. *Energy & Environmental Science* **2014**, *7*, 2448.

(4) Park, N. G. *J Phys Chem Lett* **2013**, *4*, 2423.

(5) Snaith, H. J. *J Phys Chem Lett* **2013**, *4*, 3623.

(6) Zhao, Y. X.; Zhu, K. *Chem Soc Rev* **2016**, *45*, 655.

(7) Amat, A.; Mosconi, E.; Ronca, E.; Quarti, C.; Umari, P.; Nazeeruddin, M. K.; Gratzel, M.; De Angelis, F. *Nano Lett* **2014**, *14*, 3608.

(8) Stoumpos, C. C.; Malliakas, C. D.; Kanatzidis, M. G. *Inorg Chem* **2013**, *52*, 9019.

(9) Frost, J. M.; Butler, K. T.; Brivio, F.; Hendon, C. H.; van Schilfgaarde, M.; Walsh, A. *Nano Lett* **2014**, *14*, 2584.

(10) Frost, J. M.; Butler, K. T.; Walsh, A. *Apl Materials* **2014**, *2*.

(11) Sherkar, T. S.; Koster, L. J. A. *Phys Chem Chem Phys* **2016**, *18*, 331.

(12) Eperon, G. E.; Stranks, S. D.; Menelaou, C.; Johnston, M. B.; Herz, L. M.; Snaith, H. J. *Energy & Environmental Science* **2014**, *7*, 982.

(13) Knop, O.; Wasylishen, R. E.; White, M. A.; Cameron, T. S.; Vanoort, M. J. M. *Canadian Journal of Chemistry-Revue Canadienne De Chimie* **1990**, *68*, 412.

(14) Onodayamamuro, N.; Matsuo, T.; Suga, H. *J Phys Chem Solids* **1990**, *51*, 1383.

(15) Poglitsch, A.; Weber, D. *Journal of Chemical Physics* **1987**, *87*, 6373.

(16) Onodayamamuro, N.; Matsuo, T.; Suga, H. *J Phys Chem Solids* **1992**, *53*, 935.

(17) Leguy, A. M. A.; Frost, J. M.; McMahon, A. P.; Sakai, V. G.; Kochelmann, W.; Law, C. H.; Li, X. E.; Foglia, F.; Walsh, A.; O'Regan, B. C.; Nelson, J.; Cabral, J. T.; Barnes, P. R. F. *Nat Commun* **2015**, *6*.

(18) Swainson, I. P.; Stock, C.; Parker, S. F.; Van Eijck, L.; Russina, M.; Taylor, J. W. *Physical Review B* **2015**, *92*.

(19) Bakulin, A. A.; Selig, O.; Bakker, H. J.; Rezus, Y. L. A.; Muller, C.; Glaser, T.; Lovrincic, R.; Sun, Z. H.; Chen, Z. Y.; Walsh, A.; Frost, J. M.; Jansen, T. L. C. *J Phys Chem Lett* **2015**, *6*, 3663.

(20) Juarez-Perez, E. J.; Sanchez, R. S.; Badia, L.; Garcia-Belmonte, G.; Kang, Y. S.; Mora-Sero, I.; Bisquert, J. *J Phys Chem Lett* **2014**, *5*, 2390.

(21) Kutes, Y.; Ye, L. H.; Zhou, Y. Y.; Pang, S. P.; Huey, B. D.; Padture, N. P. *J Phys Chem Lett* **2014**, *5*, 3335.

(22) Zheng, F.; Takenaka, H.; Wang, F. G.; Koocher, N. Z.; Rappe, A. M. *J Phys Chem Lett* **2015**, *6*, 31.

(23) Baumann, A.; Tvingstedt, K.; Heiber, M. C.; Vath, S.; Momblona, C.; Bolink, H. J.; Dyakonov, V. *Apl Materials* **2014**, *2*.

(24) Snaith, H. J.; Abate, A.; Ball, J. M.; Eperon, G. E.; Leijtens, T.; Noel, N. K.; Stranks, S. D.; Wang, J. T. W.; Wojciechowski, K.; Zhang, W. *J Phys Chem Lett* **2014**, *5*, 1511.

(25) Wei, J.; Zhao, Y. C.; Li, H.; Li, G. B.; Pan, J. L.; Xu, D. S.; Zhao, Q.; Yu, D. P. *J Phys Chem Lett* **2014**, *5*, 3937.

(26) Quarti, C.; Mosconi, E.; De Angelis, F. *Chem Mater* **2014**, *26*, 6557.

(27) Milot, R. L.; Eperon, G. E.; Snaith, H. J.; Johnston, M. B.; Herz, L. M. *Advanced Functional Materials* **2015**, *25*, 6218.

(28) Langevin, P. *Ann Chim Phys* **1903**, *28*, 433.
(29) Warman, J. M.; Gelinck, G. H.; de Haas, M. P. *Journal of Physics-Condensed Matter* **2002**, *14*, 9935.
(30) Warman, J. M.; de Haas, M. P.; Dicker, G.; Grozema, F. C.; Piris, J.; Debije, M. G. *Chem Mater* **2004**, *16*, 4600.
(31) Grozema, F. C. Doctoral Thesis, Delft University of Technology, 2003.
(32) Madjet, M. E. A.; Akimov, A. V.; El-Mellouhi, F.; Berdiyorov, G. R.; Ashhab, S.; Tabet, N.; Kais, S. *Phys Chem Chem Phys* **2016**, *18*, 5219.
(33) Savenije, T. J.; Ferguson, A. J.; Kopidakis, N.; Rumbles, G. *J Phys Chem C* **2013**, *117*, 24085.
(34) Hoke, E. T.; Slotcavage, D. J.; Dohner, E. R.; Bowring, A. R.; Karunadasa, H. I.; McGehee, M. D. *Chem Sci* **2015**, *6*, 613.
(35) Eames, C.; Frost, J. M.; Barnes, P. R. F.; O'Regan, B. C.; Walsh, A.; Islam, M. S. *Nat Commun* **2015**, *6*.
(36) Wehrenfennig, C.; Eperon, G. E.; Johnston, M. B.; Snaith, H. J.; Herz, L. M. *Adv Mater* **2014**, *26*, 1584.
(37) Savenije, T. J.; Ponseca, C. S.; Kunneman, L.; Abdellah, M.; Zheng, K. B.; Tian, Y. X.; Zhu, Q. S.; Canton, S. E.; Scheblykin, I. G.; Pullerits, T.; Yartsev, A.; Sundstrom, V. *J Phys Chem Lett* **2014**, *5*, 2189.
(38) Ponseca, C. S.; Savenije, T. J.; Abdellah, M.; Zheng, K. B.; Yartsev, A.; Pascher, T.; Harlang, T.; Chabera, P.; Pullerits, T.; Stepanov, A.; Wolf, J. P.; Sundstrom, V. *Journal of the American Chemical Society* **2014**, *136*, 5189.
(39) Hutter, E. M.; Eperon, G. E.; Stranks, S. D.; Savenije, T. J. *J Phys Chem Lett* **2015**, *6*, 3082.
(40) Klein, C. A. *Journal of Applied Physics* **1968**, *39*, 2029.
(41) Alig, R. C.; Bloom, S. *Physical Review Letters* **1975**, *35*, 1522.
(42) Neamen, D. A. *Semiconductor Physics and Devices: Basic Principles*; McGraw-Hill International Edition, 2012.
(43) Karakus, M.; Jensen, S. A.; D'Angelo, F.; Turchinovich, D.; Bonn, M.; Canovas, E. *J Phys Chem Lett* **2015**, *6*, 4991.
(44) Ma, J.; Wang, L. W. *Nano Lett* **2015**, *15*, 248.
(45) Berdiyorov, G. R.; El-Mellouhi, F.; Madjet, M. E.; Alharbi, F. H.; Rashkeev, S. N. *Appl Phys Lett* **2016**, *108*.
(46) Rashkeev, S. N.; El-Mellouhi, F.; Kais, S.; Alharbi, F. H. *Sci Rep-Uk* **2015**, *5*.
(47) Eperon, G. E.; Paterno, G. M.; Sutton, R. J.; Zampetti, A.; Haghighirad, A. A.; Cacialli, F.; Snaith, H. J. *J Mater Chem A* **2015**, *3*, 19688.
(48) Stoumpos, C. C.; Malliakas, C. D.; Peters, J. A.; Liu, Z. F.; Sebastian, M.; Im, J.; Chasapis, T. C.; Wibowo, A. C.; Chung, D. Y.; Freeman, A. J.; Wessels, B. W.; Kanatzidis, M. G. *Cryst Growth Des* **2013**, *13*, 2722.
(49) Jiang, C. S.; Yang, M. J.; Zhou, Y. Y.; To, B.; Nanayakkara, S. U.; Luther, J. M.; Zhou, W. L.; Berry, J. J.; van de Lagemaat, J.; Padture, N. P.; Zhu, K.; Al-Jassim, M. M. *Nat Commun* **2015**, *6*.
(50) Green, M. A. *Prog Photovoltaics* **2015**, *23*, 1202.
(51) Stranks, S. D.; Burlakov, V. M.; Leijtens, T.; Ball, J. M.; Goriely, A.; Snaith, H. J. *Physical Review Applied* **2014**, *2*.
(52) Leijtens, T.; Stranks, S. D.; Eperon, G. E.; Lindblad, R.; Johansson, E. M. J.; McPherson, I. J.; Rensmo, H.; Ball, J. M.; Lee, M. M.; Snaith, H. J. *Acs Nano* **2014**, *8*, 7147.
(53) Ulbricht, R.; Hendry, E.; Shan, J.; Heinz, T. F.; Bonn, M. *Reviews of Modern Physics* **2011**, *83*, 543.

Experimental

Materials. All chemicals were purchased from Sigma-Aldrich and used as received unless otherwise stated. CH_3NH_3I (MAI) and CH_3NH_3Br (MABr) were prepared by reacting 43.3 ml of CH_3NH_2 (40wt. % in H_2O) with 66.0 ml of HI (57wt. % in water) or 56.6 ml of HBr (48wt. % in water), respectively. The reactions were carried out in a round bottom flask placed in an ice bath for 3 hours with stirring. The precipitates were collected by rotary evaporation at 60^{o}C for 1 h. Finally, the products were washed with diethyl ether, and dried at 60^{o}C in vacuum oven overnight. PbI_2 was recrystallized with ultrapure H_2O and dried in vacuum at 90^{o}C overnight before use.

Synthesis. $CH_3NH_3PbX_3$ (X= I, Br, Cl) perovskites were prepared by reacting equivalent molar amount (2 mmol) of CH_3NH_3X and PbX_2 (X = I, Br, Cl). The starting materials were placed in

an agate mortar and ground until a visually homogeneous color powder was obtained. The ground product was then loaded in a 13 mm quartz tube, evacuated and sealed at 10^{-4} mbar. The sealed quartz tube was placed in a 200^{o}C sand bath in a fashion that the perovskite material-containing portion of the tube stays inside and the empty portion of the tube stays outside of the sand bath. The sand bath annealing process was carried out for 8 h to separate the unreacted organic starting material from the wanted homogeneous perovskite powder.

PR-TRMC measurements. A small amount of material (~45 mg) is placed in a polyimide holder and filled by pouring droplets of poly methyl methacrylate (PMMA) dissolved in chlorobenzene at a concentration of 10mg/ml every 10 min until the perovskite material is fully covered by PMMA. Then, the sample holder is left overnight to ensure the complete evaporation of the solvent. The PMMA filling is done in order to protect the samples from moisture and air and diminish the background conductivity of the material (which affects the PR-TRMC measurements). The cavity of the polyimide holder is 6x3x2 mm^3. The polyimide block with the perovskite sample is placed inside a rectangular waveguide copper cell of 14 mm length and 7.1x3.55 mm^2 of front side. The copper top wall was reduced to 0.4 mm thickness to minimize the attenuation of the electron beam. The walls of the cell were gold-plated via a redox exchange of copper with gold in order to make the cell chemically inert. In the PR-TRMC set up, the cell is contained in a cryostat in which the temperature can be varied between 200°C and -150°C. For the measurements, the temperature was varied between 90°C and -150°C depending on the sample. The temperature was maintained for ~15min before doing the actual measurement in order to assure the equilibrium of the system. The irradiation intensity was varied between pulse lengths of 200 ps and 2 ns for each temperature at a frequency of 32 GHz. The frequency scan fits were measured at a pulse length of 200 ps.

XRD measurements. XRD diffraction patterns were collected with a Bruker D8 Advance diffractometer (Bragg-Brentano geometry) equipped with a Co Kα X-ray tube (λ=1.78897) operated at 40kV and 40mA using a step size of 0.0092° and a time per step of 0.2 s. Samples were mounted in a top-loaded trough, which was rotated during data collection. Under these conditions the intensity of the strongest reflection was approximately 10000 counts.

DFT calculations. All DFT calculations were performed with VASP 5.3.3 using the experimentally determined structures of the different materials in their cubic symmetries. The electronic structure calculations were performed using a PBE exchange and correlation functional and the corresponding projected-augmented-wave pseudopotentials. Relativistic effects and d-orbitals were not included in the calculation. A full SCF calculation on a 10x10x10 gamma-centered grid was first performed and the resulting charge density was used to compute the band structure. The effective masses were then calculated from the curvature of the band at the desired k-point via the Effective Mass Calculator (EMC) program with 10^{-2} $Bohr^{-1}$ step size.